Energy Storage Materials 70 (2024) 103473

Contents lists available at ScienceDirect

Energy Storage Materials

journal homepage: www.elsevier.com/locate/ensm

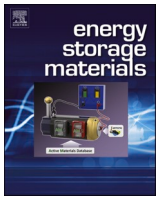

Identifying ultrathin dielectric nanosheets induced interface polarization for high-performance solid-state lithium metal batteries

Li Yang [a], Baowen Li [a], Hexing Liu [a], Hong Zhang [a], Yu Cheng [a], Qi Li [d,*], Liqiang Mai [a,b,c], Lin Xu [a,b,c,*]

[a] State Key Laboratory of Advanced Technology for Materials Synthesis and Processing, School of Materials Science and Engineering, Wuhan University of Technology, Wuhan 430070 Hubei, PR China
[b] Hubei Longzhong Laboratory, Wuhan University of Technology (Xiangyang Demonstration Zone), Xiangyang 441000, Hubei, China
[c] Hainan Institute, Wuhan University of Technology, Sanya 572000, China
[d] National Energy Key Laboratory for New Hydrogen-ammonia Energy Technologies, Foshan Xianhu Laboratory, Foshan 528200, PR China

ARTICLE INFO

Keywords:
Ultrathin dielectric nanosheet
Polymer electrolyte
Interface polarization
Ionic conductivity
Solid-state lithium batteries

ABSTRACT

Solid-state lithium metal batteries (SSLMBs) with polymer electrolytes are promising due to enhanced safety and high energy density, but the low ionic conductivity of polymer electrolytes and the unstable interface of lithium metal anode hinder the development of SSLMBs. Herein, we propose a unique strategy to address these challenges by coupling ultrathin high-dielectricity $Ca_2Nb_3O_{10}$ (CNO) nanosheets with PEO-based electrolyte. The interfacial polarization originating from the distortion of NbO_6 octahedra along the vertical direction of CNO nanosheets is maximized and so the interaction between CNO and LiTFSI, which greatly supports the dissociation of LiTFSI and improves the ionic conductivity (2.0×10^{-4} S cm^{-1}) of the composite polymer electrolyte, compared to that without CNO. The optimized interfacial polarization effect is thoroughly demonstrated by theoretical calculation and experimental results. Moreover, due to a homogeneous, robust and LiF-rich solid electrolyte interphase film with promoted Li ion transport being formed at the lithium metal interface, the superior cycling stability (90 % capacity retention after 440 cycles at 0.5 C) and rate capability for LFP||Li full batteries are achieved. This design of composite polymer electrolyte with ultrathin dielectric nanosheet fillers demonstrates a new approach to the development of high-performance polymer electrolytes for SSLMBs.

1. Introduction

With the ongoing popularization of consumer electronics and electric vehicles, along with the extensive application of renewable energy sources in the grid, there is a growing demand for high-performance energy storage devices with high energy density, long cycle and good safety [1-6]. Solid-state lithium metal batteries (SSLMBs) with polymer electrolytes are promising candidates due to the advantages of low-cost manufacturing, lightweight, flexibility of polymer electrolytes [7-10]. However, the most commonly studied polymer matrix polyethylene oxide (PEO)-based electrolyte suffers from low ionic conductivity (IC) (10^{-6}–10^{-7} S cm^{-1}) and unstable solid-state interphase (SEI) at the lithium anode interface [11-13]. Therefore, promoting the lithium salt dissociation degree thereby enhancing the ionic conductivity of polymer electrolytes, and improving the stability of SEI derived from dissociated lithium salt anions are highly desired.

To address the above challenges, introducing inorganic fillers to polymer electrolytes is the most widely adopted strategy [14-20]. In particular, inorganic fillers with high dielectric constants have unique advantages of inducing dissociation of lithium salts [21-24] via interfacial polarization for the composite solid polymer electrolyte (CSPE). For example, the spontaneous polarization of the $BaTiO_3$ dielectric fillers with particle size 0.6–1.2 μm increased the dissociation of lithium salts, leading to a high IC of CSPE [23]. Furthermore, the $BaTiO_3$ coupled nanowires with a diameter of about 250 nm produce a built-in reverse electric field that also elevates the dissociation of lithium salt [22]. However, the dimensions of the reported inorganic dielectric fillers are in the range of tens of nanometers to a few micrometers, which is far larger than the diameter of polymer chains (1–2 nm) and the size of lithium salts, resulting in a smaller specific interface area either with the polymer chains or with lithium salts. The small specific interfacial area restricts the effect of interfacial polarization originating from the

* Corresponding author.
E-mail addresses: liqi1@xhlab.cn (Q. Li), linxu@whut.edu.cn (L. Xu).

https://doi.org/10.1016/j.ensm.2024.103473
Received 19 February 2024; Received in revised form 16 April 2024; Accepted 10 May 2024
Available online 11 May 2024

dielectric fillers to the composite polymer electrolyte, resulting in limited dissociation of the lithium salt. Moreover, most of the reported inorganic dielectric fillers are nanoparticles or polycrystalline without ordered and preferred crystal planes exposed, thus making it impossible to accurately analyze the mechanism of interactions between specific crystal planes and polymer chain segments or lithium salts. Therefore, it is highly-demanded to seek an inorganic dielectric filler with a high specific interfacial area with the polymer chain and lithium salt, together with a preferred exposed crystal plane. The above two features are expected to maximize the interfacial polarization effect of dielectric fillers to the polymer electrolyte and enable the more reliable analyses of the interfacial interaction.

Herein, we designed a novel polymer composite electrolyte by coupling ultrathin $Ca_2Nb_3O_{10}$ (CNO) nanosheets with a high dielectric constant (~210) [25] with PEO-based electrolyte to promote the dissociation of lithium salt, and obtained the greatly-improved ionic conductivity. The ultrathin CNO nanosheets with ultrahigh aspect ratio results in the greatly increased specific interfacial area and hence maximized interfacial polarization effect of CNO, thus leading to largely promoted dissociation of LiTFSI. In addition, the high specific surface area of ultrathin CNO facilitates the construction of more CNO/PEO interfaces, thus providing more pathways for lithium-ion migration. Most importantly, the ε_r values of $(Ca_2Nb_3O_{10})n$ films keep a high constant level of 210 irrespective of the film thickness, which exerts the interface polarization-induced effect even in the case of stacking [26,27]. As a result, the room temperature IC of the CSPE with ultrathin CNO nanosheets is significantly improved (2.0×10^{-4} S cm^{-1}). The underlying interfacial interaction mechanism was demonstrated by theoretical calculation and experimental analyses. Moreover, a homogeneous, robust and LiF-rich SEI [28,29] with fast Li^+ transport is formed, which enables the superior cycling stability (with a high capacity-retention rate of 90 % after 440 cycles at 0.5 C) and rate capability at 2 C for solid-state LFP||Li full battery.

2. Results and discussion

2.1. LiTFSI dissociation and Li^+ transport mechanism of electrolyte with ultrathin CNO

CNO nanosheets were prepared by solid-state sintering, ion exchange and stripping as reported in the literature [30]. The dimensions of two-dimensional ultrathin nanosheet are about 400–800 nm for width and 1000–1500 nm for length (Fig. 1A, Figure S1A, C), and the X-Ray Diffraction (XRD) pattern shows good crystallinity (Figure S1D) of CNO. The thickness of ultrathin nanosheet obtained by Atomic Force Microscopy (AFM) test is ~1.8 nm (Figure S1E), which is about the thickness

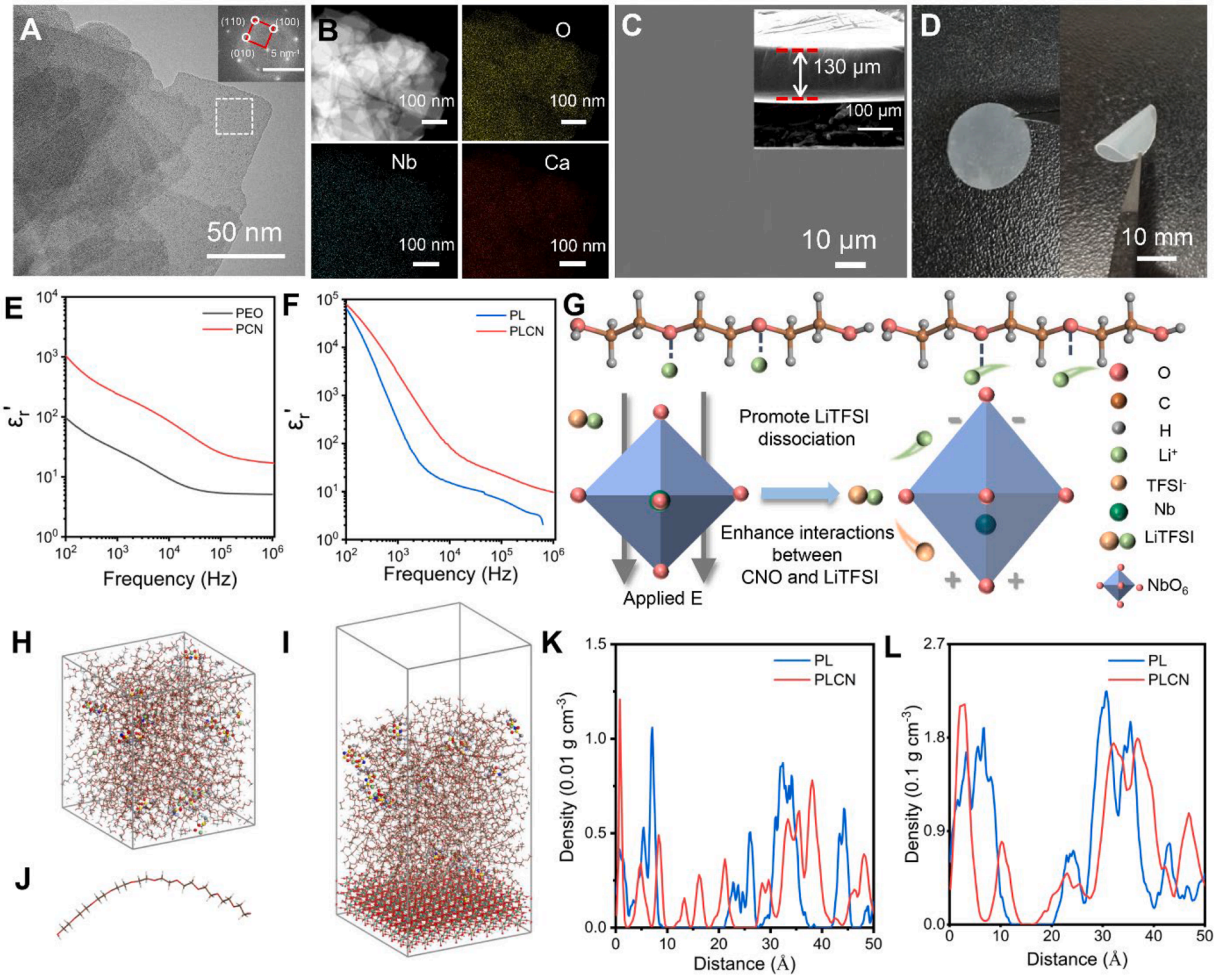

Fig. 1. Interfacial polarization-induced effect in PEO polymer electrolyte with ultrathin CNO. (A) TEM image with SAED pattern. (B) High-angle annular dark-field scanning transmission electron microscopy (HAADF-STEM) image with corresponding elemental mapping images. (C) Surficial and cross-sectional SEM images of PLCN. (D) Optical photos of PLCN. The ε_r' spectra of pure (E) PEO, PCN and (F) PL, PLCN. (G) Schematic diagrams of promoted LiTFSI dissociation via interfacial polarization in PLCN electrolyte. Snapshots of (H) PL and (I) PLCN with MD simulation. (J) PEO single chain used in MD simulation. Density distribution of (K) Li^+ and (L) $TFSI^-$ along vertical direction in PL and PLCN electrolyte system. (The white, green, brown, blue, red, gray, yellow, indigo, cyan balls represent H, Li, C, N, O, F, S, Ca, and Nb atoms, respectively. The yellow and blue regions denote the electronic depletion and accumulation, respectively).

of three NbO_6 octahedron. Besides that, the selected area electron diffraction (SAED) could be indexed to be (100), (010) and (110) planes (inset of Fig. 1A), which is consistent with the lattice plane data of high-resolution transmission electron microscope (HRTEM) (Figure S1B). Both XPS spectra (Figure S2) and energy dispersive spectral (EDS)-mapping spectra (Fig. 1B) confirm the existence of Ca, Nb, and O elements in CNO nanosheets. The commendable dispersion of CNO nanosheet in anhydrous acetonitrile (Figure S3) demonstrates its monodisperse nature and so enables the ultrathin CNO nanosheets to be evenly-distributed in polymer electrolyte. The PEO/LiTFSI/xCNO

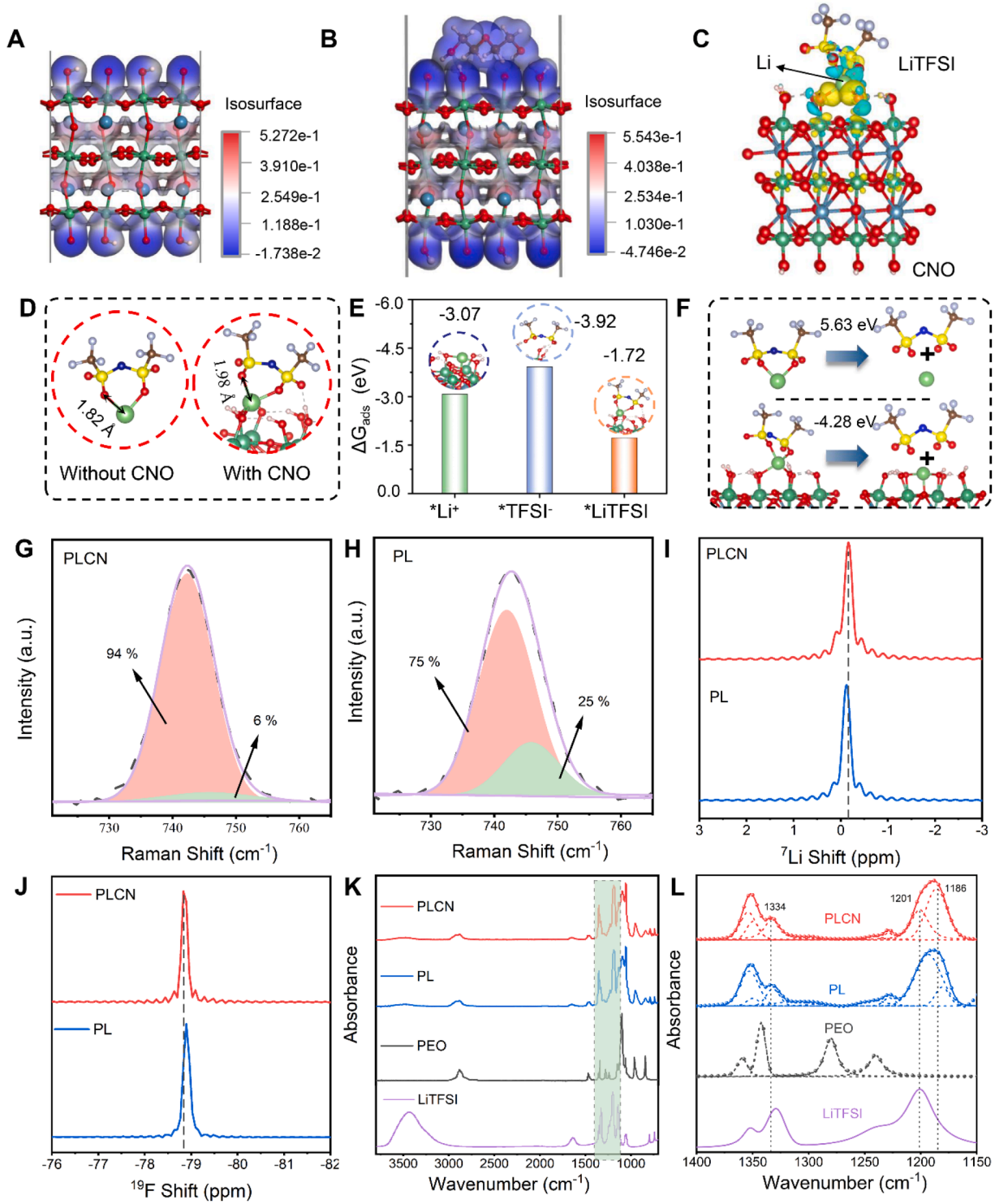

Fig. 2. The mechanism of LiTFSI dissociation in electrolyte with ultrathin CNO nanosheets. The ESP of (A) CNO and (B) CNO/TFSI. (C) Charge density difference of CNO with adsorbed LiTFSI. (D) The distance between Li and O in free LiTFSI molecular and LiTFSI with CNO. (E) The adsorption energy of Li^+, $TFSI^-$, and LiTFSI on the surface of CNO. The insets are the corresponding adsorption configuration. (F) The energy of decomposing LiTFSI into Li^+ and $TFSI^-$. Raman spectra of (G) PLCN and (H) PL. SSNMR (I) ^{7}Li and (J) ^{19}F spectra of PLCN and PL. ATR-FTIR spectra for LiTFSI, pure PEO, PL electrolyte and PLCN electrolyte at (K) 3800–700 cm^{-1} and (L) 1400–1150 cm^{-1}. (The white, green, brown, blue, red, gray, yellow, indigo, cyan balls represent H, Li, C, N, O, F, S, Ca, and Nb atoms, respectively. The yellow and blue regions denote the electronic depletion and accumulation, respectively).

electrolyte (PCNx, x represents the mass percentage of CNO relative to PEO) were prepared by coupling CNO nanosheets with PEO-based electrolyte. The PEO/LiTFSI (PL) electrolyte without CNO nanosheets was prepared as control group. Additionally, the surface of PLCN and PL electrolyte are smooth with a similar average thickness of 130–140 μm (Fig. 1C, Figure S4A, B). The cross-sectional SEM & EDS-mapping and ultrathin section TEM images of PLCN electrolyte exhibit a uniform distribution of CNO nanosheets in the PEO-based electrolyte with random directions (Figure S5, Figure S6). Optical photographs of the PLCN display that the electrolyte film is dense, semi-transparent, and has excellent flexibility (Fig. 1D).

To clarify the effect of inorganic dielectric fillers on ion transport of polymer electrolyte, the dielectric constants of polymer materials are compared before and after the addition of fillers. The PEO/CNO (PCN) composite material and PEO/LiTFSI/5CNO (PLCN) (5CNO representing 5% wt. CNO to PEO) composite electrolyte both exhibit greatly improved dielectric constant (ε_r') after introducing CNO [31,32] (Fig. 1E, F), compared to PEO and PL, respectively. According to the Born-Lande formula (1) for calculating the lattice energy of ionic compounds based on the electrostatic theory, a medium with a high dielectric constant (indicating the medium's ability to separate opposing charges from each other) weakens the attraction between oppositely charged ions in the medium, resulting in "ion-dipole bond" that makes it easier to dissociate the lithium salt. Therefore, dissociation of lithium salt will be much easier due to reduced lattice energy of lithium salt in the high dielectric constant system [33].

$$E = -\frac{AN_A z_1 z_2 e^2}{4\pi\varepsilon_0 r}\left(1-\frac{1}{n}\right) \quad (1)$$

where N_A, A, n, ε_0, r, -Z_1e and +Z_2e are the Avagadro constant (6.203×10^{23}), Medelung constant, Born index, dielectric constant, the distance between ions, and the charges of anions and cations respectively.

The increased dielectric constant of the composite system is mainly due to interfacial polarization effect between the inorganic fillers and the polymer [34-37]. The interfacial polarization effect originating from the distortion of NbO_6 octahedral in CNO causes the accumulation of dipoles at the interface between CNO and PEO, which is conducive to promote the dissociation of LiTFSI and enhance the interactions between LiTFSI and CNO (Fig. 1G). To understand the effect of CNO on LiTFSI dissociation, the molecular dynamics (MD) and density functional theory (DFT) analysis of the electrolyte with and without CNO are carried out. Based on the same PEO reference plane, we found that more Li^+ and $TFSI^-$ are distributed closer to the CNO/PEO interface in the PLCN system. This means that the dissociation of LiTFSI is enhanced at the PEO/CNO interface due to the stronger ion-dipole bond between either Li^+ or $TFSI^-$ and CNO, originating from interfacial polarization of CNO, which promotes the migration of Li^+ at the PEO/CNO interface and enhances the IC (Figure S7, Fig. 1H-L).

Furthermore, the difference in electrostatic potential (ESP) for pure CNO and CNO with $TFSI^-$ shows that the ESP is more negative when $TFSI^-$ approach to CNO, which means the strong electrostatic interaction between $TFSI^-$ and CNO (Fig. 2A, B). In addition, the ESP of CNO and PEO also changed due to the interactions of Li^+ with the nucleophilic centers of CNO and PEO (Figure S8). The interactions of CNO with LiTFSI can also be observed by differential charge density (Fig. 2C, Figure S9). As LiTFSI molecule approaches to the surface of CNO (001) plane, charge transfer occurs between Li atom in LiTFSI and O atom in CNO, which evidences the strong electronic interactions between LiTFSI and CNO. The enhanced interactions between CNO and LiTFSI is favorable to weaken the electrostatic interaction between Li^+ and $TFSI^-$, as well as to reduce the coupling between Li^+ and PEO polymer chains, which is beneficial to improve the IC (2.0×10^{-4} S cm^{-1}) (Fig. 1G, Figure S10A). In comparison, LiTFSI cannot be fully dissociated in the PL owing to the strong electrostatic attraction between Li^+ and $TFSI^-$ (Figure S10B), leading to the appearance of more LiTFSI clusters and lower IC (4.4×10^{-6} S cm^{-1}).

In addition, it is noticed that the distance between O and Li in LiTFSI increases to 1.98 Å compared to 1.82 Å in vacuum because of the existence of CNO (Fig. 2D), suggesting that the dissociation of LiTFSI is easier in PLCN. Moreover, both higher adsorption energy (−3.92 eV) between $TFSI^-$and CNO and lower dissociation energy of LiTFSI (−4.28 eV) (Fig. 2E, F) also illustrates that LiTFSI is easier to dissociate with CNO. In summary, the theoretical calculation results demonstrate the feasibility of CNO to promote LiTFSI dissociation due to the interactions between CNO and LiTFSI from the kinetic and thermodynamic perspectives, which fit well with the following experimental conclusions. To further elucidate the mechanism of interfacial polarization of CNO promoting LiTFSI dissociation, the dissociation degree of LiTFSI was thoroughly studied by Raman spectroscopy (Fig. 2G, H and Figure S11). The peaks at 743 cm^{-1} and 746 cm^{-1} are related to free $TFSI^-$ and ion-clusters respectively, and the ratio of free $TFSI^-$ represents the dissociation degree of the LiTFSI [38]. PLCN reveals a higher LiTFSI dissociation degree as illustrated in the statistical results for different CSPE systems in Figure S11D. To understand the effect of interfacial polarization-induced effects on the local chemical environment of LiTFSI, solid-state nuclear magnetic resonance spectra (SSNMR) of ^{7}Li and ^{19}F were conducted as shown in Fig. 2I, J. The ^{7}Li signal of PLCN shifts to an up-field compared to PL, suggesting a weakened interactions between PEO and LiTFSI after the introduction of CNO [39,40]. And the shift of ^{19}F spectrum also illustrates the interaction between CNO and LiTFSI. In addition, the blue shifts of -SO_2 asymmetric stretching (1331 cm^{-1}) and the -CF_3 asymmetric stretching (1193, 1180 cm^{-1}) in attenuated total reflection fourier transform infrared (ATR-FTIR) of PLCN electrolyte also suggest the strong interaction between CNO and LiTFSI (Fig. 2K, L) [41]. Moreover, the shift of the Li 1 s binding energy illustrates the weakened electrostatic attraction between Li^+ and $TFSI^-$ (Figure S12) [39]. The above results show that introduction of CNO promotes dissociation of LiTFSI through strong dipole-ion interactions between them induced by the strong interfacial polarization of ultrathin CNO nanosheet, which are consistant with the above DFT and MD simulation results.

2.2. Physicochemical properties and electrochemical performance of polymer electrolyte with ultrathin CNO

Lithium-ion migration in the PEO polymer matrix mainly occurs through complexation and de-complexation of Li^+ with oxygen on the ether-oxygen bond in PEO [42]. The slow segment movement of the highly crystalline region of PEO limits the transport of lithium ions, giving it a lower ion conductivity. The crystallization behavior of PLCN was tested by XRD, and the intensity of two specific characteristic peaks of PEO at 19.6 and 23.5 ° (Fig. 3A) in the PLCN is significantly lower than that in PL, demonstrating the increase of amorphous region after adding CNO. The XRD patterns of PL with different mass ratio of CNO also indicate the lower crystallinity (Figure S13A) after CNO being added, which is verified by the results of DSC curves (Fig. 3C). In addition, the relaxation peak of tanδ which represents the motion of ionic coupling synergistic polymer segments [43,44] (Figure S13B), PLCN exhibits the higher relaxation peak frequency than that of PL and pure PEO, which manifests the excellent polymer segment dynamics of PLCN [44]. Moreover, a lower T_g (−50.5 °C) of PLCN compared with PL (−44.8 °C) also shows the enhancement of segmental movement in PLCN (Fig. 3B). These results demonstrate the increase of amorphous region of PEO after the introduction of CNO nanosheets, which allows a much easier migration of lithium ions. In addition, the PLCN also demonstrates the enhanced thermal stability as shown in TG curves (Figure S13C) and the enhanced strength as shown in stress-strain curves (Figure S14) compared with PEO electrolyte after the addition of CNO nanosheets to PEO polymer matrix, which is beneficial to suppress the growth of lithium dendrites.

After addition of ultrathin CNO nanosheets, the PLCN electrolyte

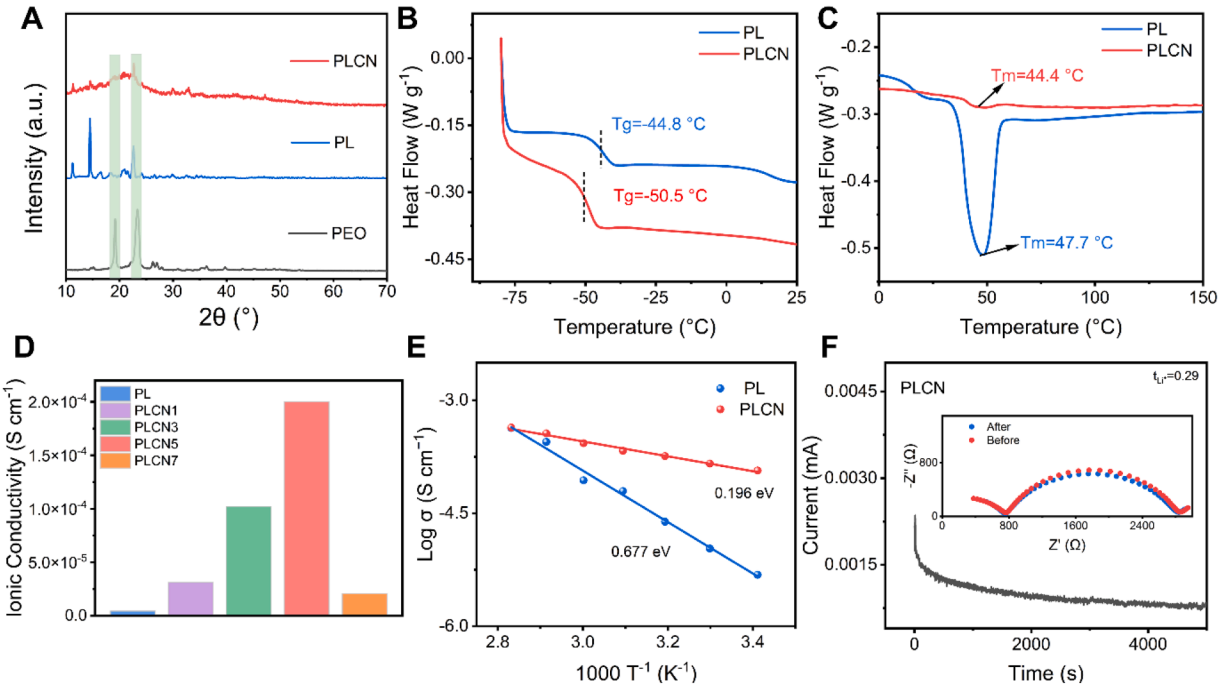

Fig. 3. Characterization of PLCN electrolyte with ultrathin CNO. (A) XRD patterns of pure PEO, PL, and PLCN. (B, C) DSC curves of PL and PLCN films. (D) The IC of PL and PLCNx (x = 1, 3, 5, 7% wt.) at room temperature. (E) Arrhenius plots of PL and PLCN. (F) The chronoamperometry curves of PLCN at room temperature, and insert figure is the corresponding EIS curves before and after polarization.

appears a significantly-enhanced IC (2.0×10^{-4} S cm^{-1}) compared with PL (4.4×10^{-6} S cm^{-1}). The IC of PLCN also stands out among PLCNx with various ratios of CNO at room temperature (Fig. 3D, Figure S15A) and at 60 °C (Figure S15B, C). It is believed that the improvement in IC originates from accelerated LiTFSI dissociation and decrease of PEO crystallinity due to the introduction of CNO. Nevertheless, with the addition of CNO, IC of PLCNx first increases and reaches the highest at 5% wt. and then decreases at 7% wt., which is probably due to the stacking of ultrathin CNO nanosheets. In particular, the stacked CNO nanosheets limit the improvement of the ionic conductivity in two aspects. On one hand, stacked CNO nanosheets lead to a decrease in their contact area with PEO and lithium salt, which makes the interfacial polarization effect much weaker. On the other hand, the decrease of the organic/inorganic interface in the composite solid-state electrolyte will lead to the blockage of ion transport channels, which is not conducive to the migration of lithium ions along the interface. It is also worth noting from the temperature-dependent EIS that the impedance of both PLCN and PL decreases with temperature due to the more intensive movement of the polymer chain (Figure S16A, B). Moreover, Arrhenius plots of PLCN, PL (Fig. 3E) and other PLCNx with different content of CNO (Figure S16C) are evaluated as well. The activation energies of different systems (inset table of Figure S16 C) were obtained by the classical Arrhenius formula. The lower the E_a, the lower the ion transport energy barrier [45]. In order to illustrate the advantages of CNO in PLCN, the CSPE with typical barium titanate dielectric (BTO) dielectric oxide materials with high dielectric constant was prepared as a comparison. The room-temperature ionic conductivity of electrolyte with the same mass percent of BTO (PLBTO) is 9×10^{-6} S cm^{-1}, which is significantly smaller than that of PLCN. Besides that, the action energy of 0.538 eV in PLBTO is larger than that of PLCN, indicating the difficulty of Li^+ transportation in PLBTO. The above results show the great advantages of CNO in enhancing ionic conductivity (Figure S17). The calculated activation energy (0.196 eV) of PLCN electrolyte is significantly smaller than that of PL (0.677 eV), suggesting a faster ion transport in PLCN. In pure PEO-based electrolytes, lithium ions migrate mainly through the ether-oxygen bonds on the PEO chain segments, which results in slow migration due to the strong bonding of lithium ions with PEO, thus resulting in a high activation energy for lithium-ion migration. However, in the PLCN electrolyte, the electrons around the O at one end away from Nb are enriched due to the shift of Nb in the NbO_6 octahedron caused by the interfacial polarization-induced effect, which enhances its interaction with the lithium ions being bound to the C—O of PEO. This interaction can weaken the adsorption of Li^+ by the C—O of PEO, thereby greatly reducing the activation energy of lithium-ion migration, and ultimately improving the IC of the PEO-based electrolyte (Figure S18). In addition, as demonstrated by the MD results, the migration rate of lithium ions at the PEO/CNO interface is faster than that at the PEO chain segments, which also contributes to lowering the activation energy of lithium-ion migration. Additionally, not only is the Li^+ transference number of PLCN at room temperature superior to that of other PEO-based electrolytes (t_{Li}^+ (PLCN) = 0.29 vs. t_{Li}^+ (PL) = 0.10) (Fig. 3F, Figure S19), but also the Li^+ transference number increases at elevated temperatures (t_{Li}^+ (60 °C) = 0.45 vs. t_{Li}^+ (25 °C) = 0.29) (Figure S20). The Li^+transference number evaluates the migration ability of lithium ions in the system, and is generally expressed by the ratio of the lithium ions to the total number of ions in the system. Therefore, a high Li^+ transference number favors the enhancement of IC (Figure S19, 20, Fig. 3H, J and Figure S15). Furthermore, a wide electrochemical window of PLCN system (4.8 V) than that of PL (3.8 V) (Figure S21) guaranteed possibility of matching with NCM811 cathode.

2.3. Solid-state lithium metal battery performances of PLCN electrolyte

The plating/striping process was conducted to assess the interface compatibility between lithium metal and electrolyte. The Li||Li symmetric cell with PLCN electrolyte achieves stable charge-discharge profiles at 0.1 mA cm^{-2} (more than 1200 h) and higher current densities without notable signs of short-circuiting at 60 °C, indicating a satisfactory interface compatibility between lithium metal and PLCN electrolyte (Fig. 4A, B). As a sharp comparison, the Li||Li symmetric cells with PL electrolyte and other PLCNx (x = 1, 3, 7) electrolyte exhibit a higher over-potential and an abrupt short-circuiting after shorter time,

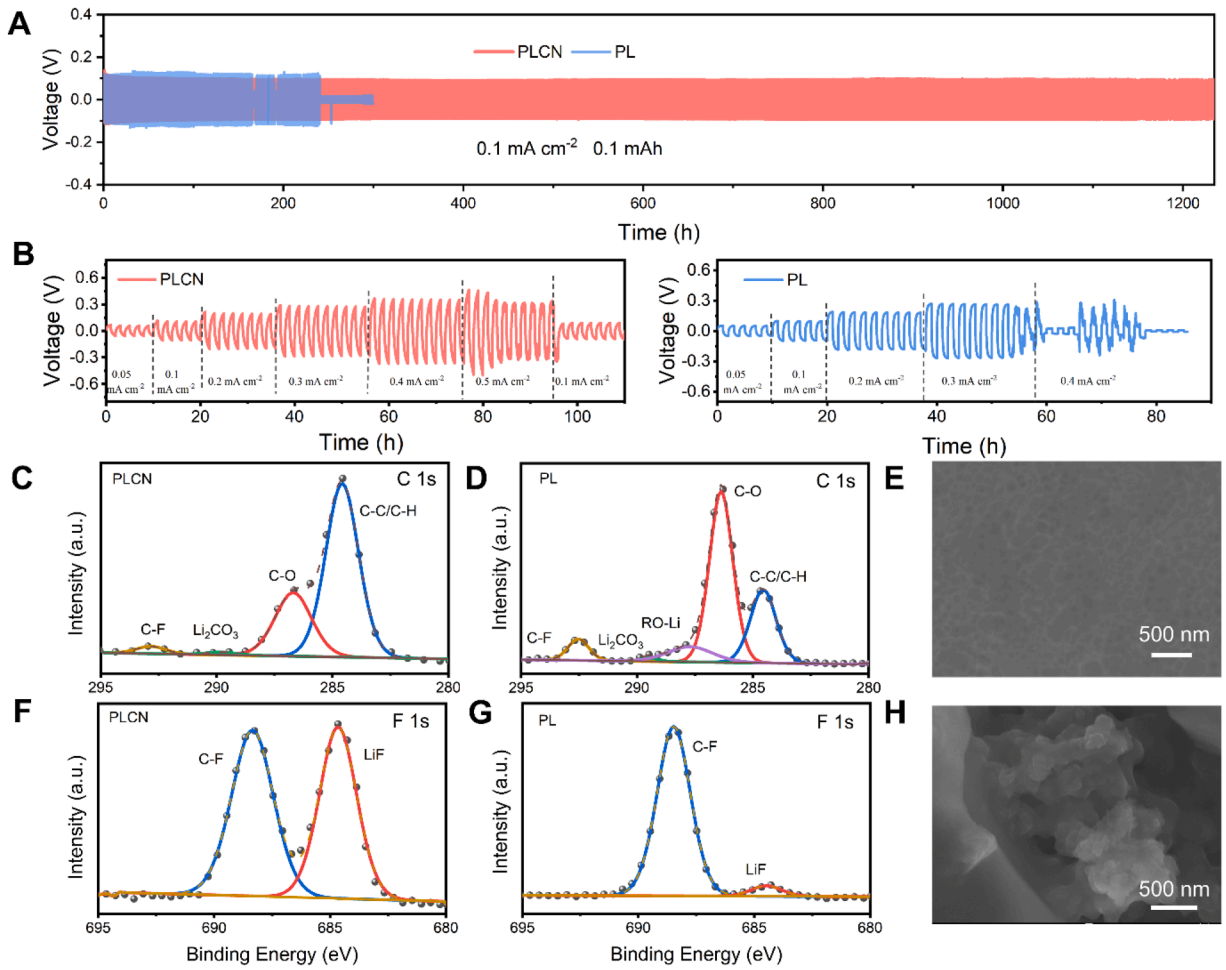

Fig. 4. Solid-state cell performances of PLCN electrolyte. (A) The voltage-time profiles of lithium plating/stripping cycles of Li||Li symmetric cells at 0.1 mA cm^{-2} and 60 °C. (B) Voltage-time profiles of Li||(PLCN)||Li and Li||(PL)||Li cells at 0.05, 0.1, 0.2, 0.3, 0.4 and 0.5 mA cm^{-2} with capacity of 0.05, 0.1, 0.2, 0.3, 0.4 and 0.5 mAh cm^{-2} respectively at 60 °C. C 1 s XPS spectra for Li electrode obtained from (C) Li||(PLCN)||Li and (D) Li||(PL)||Li symmetric cells after cycling 120 h. F 1 s XPS spectra for Li electrode obtained from (F) Li||(PLCN)||Li and (G) Li||(PL)||Li symmetric cells after cycling 120 h. The surface morphology and the corresponding interface diagrams of Li electrode obtained from (E) Li||(PLCN)||Li and (H) Li||(PL)||Li symmetric cells after cycling 120 h.

illustrating a poor interfacial stability and the failure of SPE for inhibiting growth of lithium dendrites (Fig. 4A, Figure S22). The excellent plating/stripping features of Li||Li symmetrical cells with PLCN electrolyte are attributed to a better interfacial stability between lithium metal and PLCN after the introduction of CNO nanosheets. To illustrate the interfacial stability between the composite solid-state electrolyte PLCN and lithium metal, impedance spectra of the Li||Li symmetric cells before and after cycling (100 h) are tested. The impedance of Li||Li symmetrical cell with PLCN after cycling is much lower than that before cycling, which reflects the good stability between the electrolyte and lithium anode. In contrast, the impedance of Li||Li symmetrical cell with PL increases after cycling due to the unstable interface (Figure S23). The decrease of impedance for Li||Li symmetrical cell mainly originates from the superior SEI with abundant LiF. The SEM EDS-mapping of lithium metal after cycling illustrates a uniform distribution of F element, suggesting the formation of homogeneous LiF-rich SEI (Fig. 4C-G, Figure S24A, B) which can alleviate the side reactions and suppress lithium dendrites growth at the lithium anode interface, resulting in improved cycling stability [46]. This is because CNO can trigger the easier reaction of LiTFSI at the lithium metal interface to form LiF (Figure S23) [47,48], indicated by the increased S2-N bond length in LiTFSI from 1.58 Å to 3.52 Å after coupling with CNO (Figure S25). In contrast, a rough and "dead Li"-rich interphase with massive RO-Li by-products (Fig. 4D, H, Figure S24C, D) is formed in the Li||(PL)||Li symmetric cell, indicating the serious side reactions on the lithium anode. Furthermore, the smaller impedance of Li||(PLCN)||Li cell verifies an excellent interfacial compatibility between the PLCN and the lithium electrode and the formation of an ion-conducting SEI (Figure S26) [40,49]. Specifically, the impedance of the Li||(PLCN)||Li cell first increases, then decreases, and finally stabilizes with increasing storage time at 60 °C. This result shows that the ion-conducting of SEI is slowly formed over storage time, which hinders the side reactions on the lithium anode. Herein, we can come to a conclusion that a homogeneous, smooth and LiF-rich SEI film is formed on the lithium anode, which facilitates the transport of Li ion across the interphase film and also suppresses lithium dendrite formation during the repeated Li plating/stripping process [50].

Solid-state $LiFePO_4$ (LFP)||Li full batteries with PLCN electrolyte and PL were assembled. A capacity retention rate of 90 % after 440 cycles (141 mAh g^{-1}) is achieved at 0.5 C and 60 °C with average coulombic efficiency of 99 % for the full battery with PLCN (Fig. 5A). In contrast, the discharge capacity of full battery with PL electrolyte decreases abruptly after 58 cycles (52.3 mAh g^{-1} with capacity retention rate of 35 %) (Fig. 5A). In addition, the lower polarization potential of LFP|| Li full battery with PLCN illustrate the better interfacial compatibility (Figure S27). It is noteworthy that the cycling performance of LFP||(PLCN)||Li battery at 0.2 C and 60 °C is also superior to LFP||(PL)||Li battery (Figure S28). The lower polarization potential, smooth feature

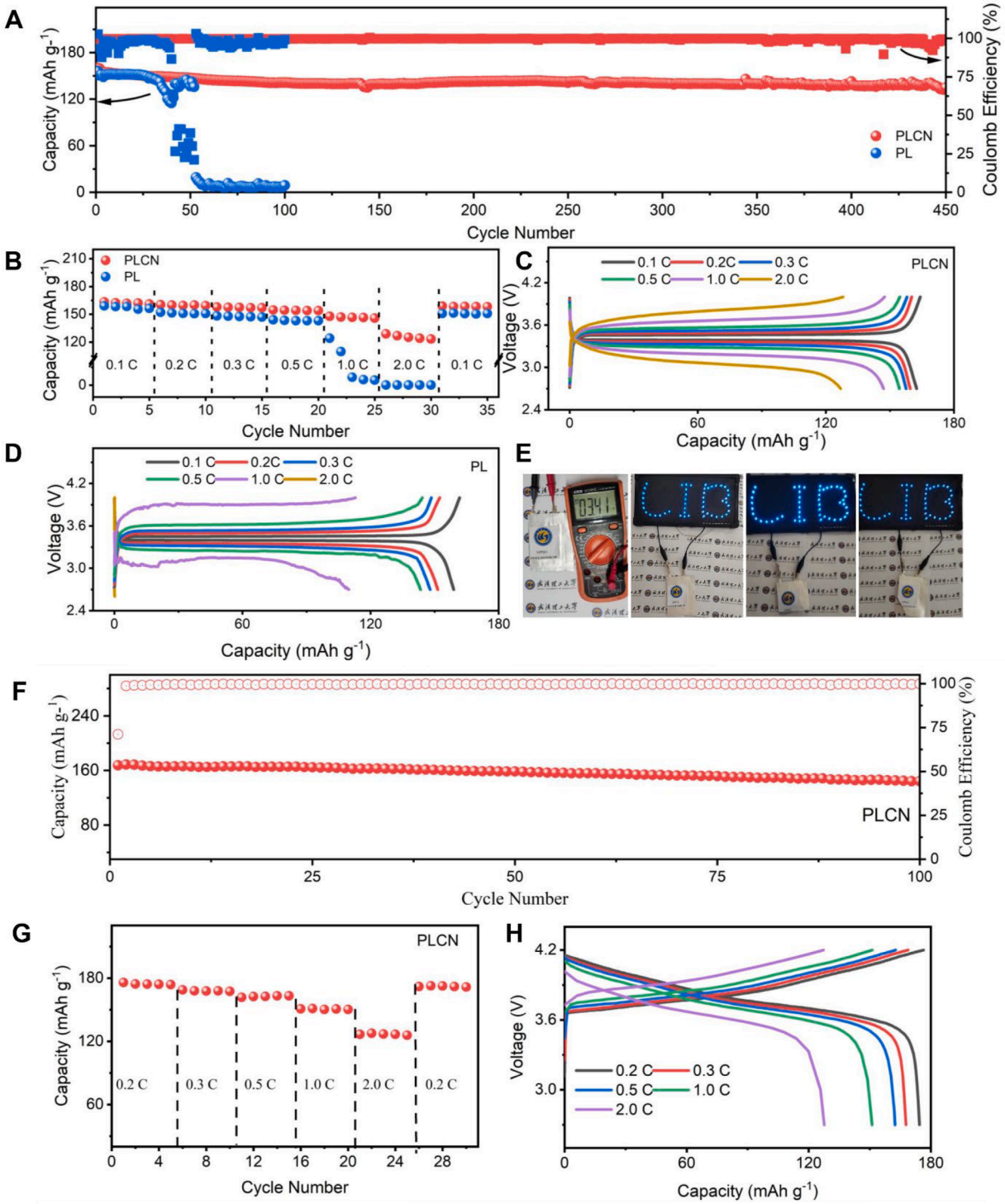

Fig. 5. Solid-state full battery performances with PLCN electrolyte. (A) Cycle performance of LFP||Li full batteries at 0.5 C and 60 °C. (B) Rate performance of LFP||Li full batteries at 60 °C. Charge-discharge curves of (C) LFP||(PLCN)||Li and (D) LFP||(PL)||Li full batteries at 0.1, 0.2, 0.3, 0.5, 1.0 and 2.0 C at 60 °C. (E) Optical photographs of the flexible LFP||(PLCN)||Li pouch battery under different states (flatting, folding and cutting), lighting up an LED in series at room temperature. (F) Cycling performance of NCM811||(PLCN)||Li battery and room temperature. (G) Rate performance and (H) charge-discharge curves of NCM811||(PLCN)||Li battery at room temperature.

and steady plateaus of charging/discharging curves in LFP|| Li full battery with PLCN demonstrates the superior interfacial polarization induced effect originating from the ultrathin CNO nanosheets in stabilizing the interface during cycling process (Figure S25). Besides that, the rate performances of LFP||(PLCN)||Li and LFP||(PL)||Li batteries (from 0.1 C to 2.0 C) were compared in Fig. 5B. The battery assembled with PLCN electrolyte delivers 162.2, 159.9, 157.4, 154.3, 146.7 and 125.6 mAh g^{-1} in average at 0.1, 0.2, 0.3, 0.5, 1.0 and 2.0 C rates respectively, which are higher than those of LFP||(PL)||Li batteries at corresponding rates, indicating a faster Li ion transport in battery with PLCN electrolyte.

And the charge-discharge curves of LFP||Li battery with PLCN

remain steady with small polarization at high rates (Fig. 5C, D), suggesting the outstanding electrochemical reaction kinetics even at high rates. Meanwhile, LFP||(PLCN)||Li battery also shows excellent capacity reversibility when the rate returns to 0.1 C because of the robust interphase with faster Li ion transport. By contrast, an average discharge capacity of the battery with PL approaches to zero at 2.0 C, which reflects the insufficient Li ion supply to the electrochemical reaction interface at high current density. The interphase morphology and composition of both lithium anode and LFP cathode after 10 cycles at 0.2 C are analyzed. A smooth and flat SEI with much inorganic components (such as LiF, Li_3N, Li_2CO_3) on the lithium anode (Figure S29, Figure S30) can be observed after 10 cycles in LFP||(PLCN)||Li battery, which is beneficial to improve cycle stability. In contrast, the formation of prominent lithium dendrites on the surface of lithium metal in LFP||(PL)||Li battery leads to its poor cycling stability (Figure S29B). Besides that, dense and smooth cathode electrolyte interphase (CEI) film composed of more LiF and Li_3N is also beneficial to improve the cycling stability for the battery with CNO (Figure S31, Figure S32). Furthermore, flexibility is an advantage for the practical application of SSLMB with polymer electrolyte. LFP||(PLCN)||Li pouch battery can light up an LED in series at room temperature in different situations (flat, folding, cutting) as shown in Fig. 5E, demonstrating its flexibility and obvious safety merits of the pouch battery in practical applications.

In addition, the cycle stability of NCM811||(PLCN)||Li battery was also evaluated at 0.5 C and room temperature, which shows a decent capacity retention of 86 % after 100 cycles (Fig. 5F). When cycling NCM811||(PLCN)||Li battery with gradually increased rates of 0.2, 0.3, 0.5, 1.0 and 2.0 C at room temperature, the full battery delivered specific capacities of 174.6, 167.9, 162.6, 150.8, and 126.7 mAh g^{-1}, respectively. The specific capacity finally recovered to 172.2 mA h g^{-1} after returning 0.2 C at room temperature, which indicates a high capacity-recovery rate of 99 % (Fig. 5G, H). Finally, the electrochemical properties of the PLCN electrolyte in this work are compared with those of recently published PEO-based electrolytes with different fillers (Figure S33). This comparison clearly shows that the overall performances of PLCN stand out among other previously reported electrolytes, including IC, lithium plating/striping reversibility, and cycling stability of LFP||Li full battery, which clearly demonstrates the overwhelming advantages of ultrathin dielectric CNO nanosheet fillers in improving the performances of PEO-based polymer composite electrolytes.

3. Conclusions

In summary, a unique polymer composite electrolyte PLCN via coupling high-dielectricity ultrathin CNO nanosheets fillers with PEO electrolyte was fabricated by a facile method, which leads to the significantly-enhanced ionic conductivity (2.0×10^{-4} S cm^{-1}), superior cycling stability and rate capability in solid-state lithium metal batteries. Comprehensive calculation and characterization results reveal the key role of the maximized interfacial polarization in promoting LiTFSI dissociation and hence ionic conductity. Moreover, the improved interaction between CNO nanosheets and LiTFSI triggers the easier reaction of LiTFSI at the lithium metal interface to in situ form a homogeneous, robust and LiF-rich SEI film with faster Li ion transport, which in turn stabilizes the electrochemical reaction interface between PLCN electrolyte and lithium metal as well as promotes the reaction kinetics. As a result, stable cycling (90 % capacity retention after 440 cycles at 0.5 C) and superior rate capability for the solid-state LFP||Li full batteries were realized. This well-designed polymer composite electrolyte with high-dielectricity ultrathin nanosheet fillers and the in-depth analyses of the interfacial polarization induced effect open up an avenue towards the rational design of other high-performance polymer electrolytes for solid-state lithium metal batteries.

Supplementary materials associated with this article is available from the ELSEVIER Online Library or from the author.

CRediT authorship contribution statement

Li Yang: Writing – review & editing, Writing – original draft, Methodology, Formal analysis, Data curation. **Baowen Li:** Data curation, Funding acquisition, Investigation, Validation. **Hexing Liu:** Data curation, Formal analysis. **Hong Zhang:** Formal analysis, Data curation. **Yu Cheng:** Data curation, Formal analysis. **Qi Li:** Writing – review & editing, Writing – original draft, Funding acquisition, Conceptualization, Data curation, Formal analysis, Resources. **Liqiang Mai:** Funding acquisition, Project administration, Resources, Supervision. **Lin Xu:** Writing – review & editing, Funding acquisition, Conceptualization, Project administration, Resources, Supervision.

Declaration of competing interest

The authors declare that they have no known competing financial interests or personal relationships that could have appeared to influence the work reported in this paper.

Acknowledgements

This work was financially supported by the National Natural Science Foundation of China (52272234, 51872214, 52072285), the National Key Research and Development Program of China (2020YFA0715000), the Key Research and Development Program of Hubei Province (2021BAA070), Independent Innovation Projects of the Hubei Longzhong Laboratory (2022ZZ-20), the Sanya Science and Education Innovation Park of Wuhan University of Technology (2021KF0011).

Supplementary materials

Supplementary material associated with this article can be found, in the online version, at doi:10.1016/j.ensm.2024.103473.

References

[1] X. Zeng, M. Li, D. Abd El Hady, W. Alshitari, A.S. Al Bogami, J. Lu, K. Amine, Commercialization of lithium battery technologies for electric vehicles, Adv. Energy Mater. 9 (2019) 1900161, https://doi.org/10.1002/aenm.201900161.
[2] R. Sahore, Z. Du, X.C. Chen, W.B. Hawley, A.S. Westover, N.J. Dudney, Practical considerations for testing polymer electrolytes for high-energy solid-state batteries, ACS Energy Lett 6 (2021) 2240–2247, https://doi.org/10.1021/acsenergylett.1c00810.
[3] Q. Wu, M. Fang, S. Jiao, S. Li, S. Zhang, Z. Shen, S. Mao, J. Mao, J. Zhang, Y. Tan, K. Shen, J. Lv, W. Hu, Y. He, Y. Lu, Phase regulation enabling dense polymer-based composite electrolytes for solid-state lithium metal batteries, Nat. Commun. 14 (2023), https://doi.org/10.1038/s41467-023-41808-3.
[4] J. Yang, R. Li, P. Zhang, J. Zhang, J. Meng, L. Li, Z. Li, X. Pu, Crosslinked polymer-in-salt solid electrolyte with multiple ion transport paths for solid-state lithium metal batteries, Energy Stor. Mater. 64 (2024) 103088, https://doi.org/10.1016/j.ensm.2023.103088.
[5] S. Guo, W. Kou, W. Wu, R. Lv, Z. Yang, J. Wang, Thin laminar inorganic solid electrolyte with high ionic conductance towards high-performance all-solid-state lithium battery, Chem. Eng. J. 427 (2022) 131948, https://doi.org/10.1016/j.cej.2021.131948.
[6] R. Lv, W. Kou, S. Guo, W. Wu, Y. Zhang, Y. Wang, J. Wang, Preparing two-dimensional ordered $Li_{0.33}La_{0.557}TiO_3$ crystal in interlayer channel of thin laminar inorganic solid-state electrolyte towards ultrafast Li^+ transfer, Angew. Chem. Int. Ed. 61 (2021) e202114220, https://doi.org/10.1002/anie.202114220.
[7] Q. Cheng, A. Li, N. Li, S. Li, A. Zangiabadi, T. Li, W. Huang, A.C. Li, T. Jin, Q. Song, W. Xu, N. Ni, H. Zhai, M. Dontigny, K. Zaghib, X. Chuan, D. Su, K. Yan, Y. Yang, Stabilizing solid electrolyte-anode interface in Li-metal batteries by boron nitride-based nanocomposite coating, Joule 3 (2019) 1510–1522, https://doi.org/10.1016/j.joule.2019.03.022.
[8] J. Hu, C. Lai, K. Chen, Q. Wu, Y. Gu, C. Wu, C. Li, Dual fluorination of polymer electrolyte and conversion-type cathode for high-capacity all-solid-state lithium metal batteries, Nat. Commun. 13 (2022), https://doi.org/10.1038/s41467-022-35636-0.
[9] H. Zhang, J. Chen, J. Liu, X. Zhang, J. Yang, Y. Nuli, H. Ma, J. Wang, Gel electrolyte with flame retardant polymer stabilizing lithium metal towards lithium-sulfur battery, Energy Stor. Mater. 61 (2023) 102885, https://doi.org/10.1016/j.ensm.2023.102885.
[10] W. Kou, R. Lv, S. Zuo, Z. Yang, J. Huang, W. Wu, J. Wang, Hybridizing polymer electrolyte with poly(ethylene glycol) grafted polymer-like quantum dots for all-

solid-state lithium batteries, J. Memb. Sci. 618 (2021) 118702, https://doi.org/10.1016/j.memsci.2020.118702.
[11] M. Dirican, C. Yan, P. Zhu, X. Zhang, Composite solid electrolytes for all-solid-state lithium batteries, Mater. Sci. Eng. R Rep. 136 (2019) 27–46, https://doi.org/10.1016/j.mser.2018.10.004.
[12] P.M. Eliana Quartarone, Aldo Magistris, PEO-based composite polymer electrolytes, Solid State Ion 110 (1998) 1–14.
[13] Z. Li, H. Zhang, X. Sun, Y. Yang, Mitigating interfacial instability in polymer electrolyte-based solid-state lithium metal batteries with 4 V cathodes, ACS Energy Lette 5 (2020) 3244–3253, https://doi.org/10.1021/acsenergylett.0c01465.
[14] Y. Li, Z. Sun, D. Liu, Y. Gao, Y. Wang, H. Bu, M. Li, Y. Zhang, G. Gao, S. Ding, A composite solid polymer electrolyte incorporating MnO_2 nanosheets with reinforced mechanical properties and electrochemical stability for lithium metal batteries, J. Mater. Chem. A 8 (2020) 2021–2032, https://doi.org/10.1039/c9ta11542k.
[15] W. Liu, N. Liu, J. Sun, P.C. Hsu, Y. Li, H.W. Lee, Y. Cui, Ionic conductivity enhancement of polymer electrolytes with ceramic nanowire fillers, Nano Lett. 15 (2015) 2740–2745, https://doi.org/10.1021/acs.nanolett.5b00600.
[16] N. Wu, P.H. Chien, Y. Li, A. Dolocan, H. Xu, B. Xu, N.S. Grundish, H. Jin, Y.Y. Hu, J. B. Goodenough, Fast Li^+ conduction mechanism and interfacial chemistry of a NASICON/polymer composite electrolyte, J. Am. Chem. Soc. 142 (2020) 2497–2505, https://doi.org/10.1021/jacs.9b12233.
[17] E.H. Cha, S.A. Lim, C.W. Lee, D.R. Macfarlane, Ionic conductance of PDMAEMA/PEO polymeric electrolyte containing lithium salt mixed with plasticizer, J. Power Sources 163 (2006) 269–273, https://doi.org/10.1016/j.jpowsour.2006.05.058.
[18] Y. Huang, T. Gu, G. Rui, P. Shi, W. Fu, L. Chen, X. Liu, J. Zeng, B. Kang, Z. Yan, F. J. Stadler, L. Zhu, F. Kang, Y. He, A relaxor ferroelectric polymer with an ultrahigh dielectric constant largely promotes the dissociation of lithium salts to achieve high ionic conductivity, Energy Environ. Sci. 14 (2021) 6021–6029, https://doi.org/10.1039/d1ee02663a.
[19] V. Vijayakumar, M. Ghosh, K. Asokan, S.B. Sukumaran, S. Kurungot, J. Mindemark, D. Brandell, M. Winter, J.R. Nair, 2D layered nanomaterials as fillers in polymer composite electrolytes for lithium batteries, Adv. Energy Mater 13 (2023) 2203326, https://doi.org/10.1002/aenm.202203326.
[20] L. Huang, H. Fu, J. Duan, T. Wang, X. Zheng, Y. Huang, T. Zhao, Q. Yu, J. Wen, Y. Chen, D. Sun, W. Luo, Y. Huang, Negating Li+ transfer barrier at solid-liquid electrolyte interface in hybrid batteries, Chem. 8 (2022) 1928–1943, https://doi.org/10.1016/j.chempr.2022.03.002.
[21] N. Angulakhsmi, B. Ambrose, S. Sathya, M. Kathiresan, G. Lingua, S. Ferrari, E. B. Gowd, W. Wang, C. Shen, G.A. Elia, C. Gerbaldi, A.M. Stephan, Enhanced electrochemical performance of hybrid solid polymer electrolytes encompassing viologen for all-solid-state lithium polymer batteries, ACS Materials Au 3 (2023) 528–539, https://doi.org/10.1021/acsmaterialsau.3c00010.
[22] P. Shi, J. Ma, M. Liu, S. Guo, Y. Huang, S. Wang, L. Zhang, L. Chen, K. Yang, X. Liu, Y. Li, X. An, D. Zhang, X. Cheng, Q. Li, W. Lv, G. Zhong, Y.-B. He, F. Kang, A dielectric electrolyte composite with high lithium-ion conductivity for high-voltage solid-state lithium metal batteries, Nat. Nanotechnol. 18 (2023) 602–610, https://doi.org/10.1038/s41565-023-01341-2.
[23] H.-J.S.H.Y. Sun, O. Yamamoto, Y. Takeda, N. Imanishic, Enhanced lithium-ion transport in PEO-based composite polymer electrolytes with ferroelectric $BaTiO_3$, J. Electrochem. Soc. 146 (1999) 1672–1676.
[24] A. Jagadeesan, M. Sasikumar, R. Jeevani, H.A. Therese, N. Ananth, P. Sivakumar, Fabrication of $BaTiO_3$ ceramic filler incorporated PVC-PEMA based blend nanocomposite gel polymer electrolytes for Li ion battery applications, J. Mater. Sci. Mater. Electron. 30 (2019) 17181–17194, https://doi.org/10.1007/s10854-019-02065-7.
[25] Y.H. Kim, H.J. Kim, M. Osada, B. Li, Y. Ebina, T. Sasaki, 2D perovskite nanosheets with thermally-stable high-kappa response: a new platform for high-temperature capacitors, ACS Appl. Mater. Interfaces 6 (2014) 19510–19514, https://doi.org/10.1021/am506629g.
[26] K.A. Minoru Osada, Yasuo Ebina, Hiroshi Funakubo, § Kanta Ono, Kazunori Takada, Takayoshi Sasaki, Robust High-κ response in molecularly thin perovskite nanosheets, ACS Nano 4 (2010) 5525–5532, https://doi.org/10.1021/nn101453v.
[27] M.O. Bao-Wen Li, Yasuo Ebina, Kosho Akatsuka, Katsutoshi Fukuda, Takayoshi Sasaki, High thermal robustness of molecularly thin perovskite nanosheets and implications for superior dielectric properties, ACS Nano 8 (2014) 5449–5461, https://doi.org/10.1021/nn502014c.
[28] B. Li, Y. Wang, S. Yang, A material perspective of rechargeable metallic lithium anodes, Adv. Energy Mater. 8 (2018) 1702296, https://doi.org/10.1002/aenm.201702296.
[29] G. Hou, X. Ma, Q. Sun, Q. Ai, X. Xu, L. Chen, D. Li, J. Chen, H. Zhong, Y. Li, Z. Xu, P. Si, J. Feng, L. Zhang, F. Ding, L. Ci, Lithium dendrite suppression and enhanced interfacial compatibility enabled by an ex situ SEI on Li anode for LAGP-based all-solid-state batteries, ACS Appl. Mater. Interfaces 10 (2018) 18610–18618, https://doi.org/10.1021/acsami.8b01003.
[30] Y. Ebina, T. Sasaki, M. Watanabe, Study on exfoliation of layered perovskite-type niobates, Solid State Ion. 151 (2002) 177–182, https://doi.org/10.1016/S0167-2738(02)00707-5.
[31] G. Jian, M. Liu, C. Yan, F. Wu, B. Song, K. Moon, C. Wong, A strategy for design of non-percolative composites with stable giant dielectric constants and high energy densities, Nano Energy 58 (2019) 419–426, https://doi.org/10.1016/j.nanoen.2019.01.037.
[32] Z. Dang, J. Yuan, J. Zha, T. Zhou, S. Li, G. Hu, Fundamentals, processes and applications of high-permittivity polymer–matrix composites, Prog. Mater. Sci. 57 (2012) 660–723, https://doi.org/10.1016/j.pmatsci.2011.08.001.
[33] Aakash Gupta, D. Jana, Modified born lande equation to calculate lattice energy in a theoretical approach, ChemRxiv (2021), https://doi.org/10.26434/chemrxiv-2021-z2n68.
[34] N. Xu, L. Hu, Q. Zhang, X. Xiao, H. Yang, E. Yu, Significantly enhanced dielectric ferformance of poly(vinylidene fluoride-co-hexafluoropylene)-based composites filled with hierarchical flower-like TiO_2 particles, ACS Appl. Mater. Interfaces 7 (2015) 27373–27381, https://doi.org/10.1021/acsami.5b08987.
[35] M. Zhang, P. Xu, H. Peng, F. Qin, A rational design of core-shell-satellite structured $BaTiO_3$ fillers for epoxy-based composites with enhanced microwave dielectric constant and low loss, Compos. Part B-Eng. 215 (2021) 108764, https://doi.org/10.1016/j.compositesb.2021.108764.
[36] Z. Xie, D. Liu, Y. Xiao, K. Wang, Q. Zhang, K. Wu, Q. Fu, The effect of filler permittivity on the dielectric properties of polymer-based composites, Compos. Sci. Technol. 222 (2022) 109342, https://doi.org/10.1016/j.compscitech.2022.109342.
[37] B. Li, M. Osada, Y.H. Kim, Y. Ebina, K. Akatsuka, T. Sasaki, Atomic layer engineering of high-kappa ferroelectricity in 2D perovskites, J. Am. Chem. Soc. 139 (2017) 10868–10874, https://doi.org/10.1021/jacs.7b05665.
[38] Z. Zhang, H. Ying, G. Zhang, L. Chao, Three-dimensional fiber network reinforced polymer electrolyte for dendrite-free all-solid-state lithium metal batteries, Energy Stor. Mater. 41 (2021) 631–641, https://doi.org/10.1016/j.ensm.2021.06.030.
[39] H. Xu, L. Huang, W. Li, S. Gu, D. Zeng, Y. Zhang, Y. Sun, H. Cheng, Shielding the electrostatic attraction by design of zwitterionic single ion conducting polymer electrolyte with high dielectric constant, J. Membr. Sci. 651 (2022) 120452, https://doi.org/10.1016/j.memsci.2022.120452.
[40] H. Xu, P.H. Chien, J. Shi, Y. Li, N. Wu, Y. Liu, Y.Y. Hu, Y. Goodenough, High-performance all-solid-state batteries enabled by salt bonding to perovskite in poly (ethylene oxide), Proc. Natl. Acad. Sci. U.S.A. 116 (2019) 18815–18821, https://doi.org/10.1073/pnas.1907507116.
[41] Y. Lin, X. Wang, J. Liu, J.D. Miller, Natural halloysite nano-clay electrolyte for advanced all-solid-state lithium sulfur batteries, Nano Energy 31 (478) (2017) 455, https://doi.org/10.1016/j.nanoen.2016.11.045.
[42] J. Atik, D. Diddens, J.H. Thienenkamp, G. Brunklaus, M. Winter, E. Paillard, Cation-assisted lithium-ion transport for high-performance PEO-based ternary solid polymer electrolytes, Angew. Chem., Int. Ed. 60 (2021) 11919–11927, https://doi.org/10.1002/anie.202016716.
[43] S. Choudhary, R.J. Sengwa, Effects of different inorganic nanoparticles on the structural, dielectric and ion transportation properties of polymers blend based nanocomposite solid polymer electrolytes, Electrochim. Acta 247 (2017) 924–941, https://doi.org/10.1016/j.electacta.2017.07.051.
[44] K.P. Sindhu, S.S.M. Abdul Majeed, J. Shahitha Parveen, PEO/PMMA solid nanocomposite polyelectrolyte with enhanced ionic conductivity and promising dielectric properties, J. Electron. Mater. 50 (2021) 6654–6666, https://doi.org/10.1007/s11664-021-09205-y.
[45] F.M. Pesci, A. Bertei, R.H. Brugge, S.P. Emge, A.K.O. Hekselman, L.E. Marbella, C. P. Grey, A. Aguadero, Establishing ultralow activation energies for lithium transport in garnet electrolytes, ACS Appl. Mater. Interfaces 12 (2020) 32806–32816, https://doi.org/10.1021/acsami.0c08605.
[46] J. Zheng, Z. Ju, B. Zhang, J. Nai, T. Liu, Y. Liu, Q. Xie, W. Zhang, Y. Wang, X. Tao, Lithium ion diffusion mechanism on the inorganic components of the solid-electrolyte interphase, J. Mater. Chemi. A 9 (2021) 10251–10259, https://doi.org/10.1039/d0ta11444h.
[47] M. Chen, J. Zheng, Y. Liu, O. Sheng, Z. Ju, G. Lu, T. Liu, Y. Wang, J. Nai, Q. Wang, X. Tao, Marrying ester group with lithium salt: cellulose-acetate-enabled LiF-enriched interface for stable lithium metal anodes, Adv. Funct. Mater. 31 (2021) 2102228, https://doi.org/10.1002/adfm.202102228.
[48] H. Zhang, C. Shen, Y. Huang, Z. Liu, Spontaneously formation of SEI layers on lithium metal from LiFSI/DME and LiTFSI/DME electrolytes, Appl. Surf. Sci. 537 (2021) 147983, https://doi.org/10.1016/j.apsusc.2020.147983.
[49] Y. Zhao, T. Zhou, L.P.H. Jeurgens, X. Kong, J.W. Choi, A. Coskun, Electrolyte engineering for highly inorganic solid electrolyte interphase in high-performance lithium metal batteries, Chem. 9 (2023) 682–697, https://doi.org/10.1016/j.chempr.2022.12.005.
[50] N. Li, Y. Shi, Y. Yin, X. Zeng, J. Li, C. Li, L. Wan, R. Wen, Y. Guo, A flexible solid electrolyte interphase layer for long-life lithium metal anodes, Angew. Chem., Int. Ed. 57 (2018) 1505–1509, https://doi.org/10.1002/anie.201710806.